ORIENTAL JOURNAL OF CHEMISTRY
An International Open Access, Peer Reviewed Research Journal
www.orientjchem.org
ISSN: 0970-020 X
CODEN: OJCHEG
2024, Vol. 40, No.(4):
Pg. 1138-1144

Hydrothermal Synthesis of Metal Sulfides (MS_2; M = Mo and W) Nanostructures with their Structural and Optical Properties

KAVITA YADAV[1], KAVITHA KUMARI[1], MANU KUMAR BHANDORIA[2], YASHPAL SHARMA[3]* and JITENDRA GANGWAR[4]*

[1]Department of Chemistry, Baba Mastnath University, Asthal Bohar, Rohtak, Haryana, 121021, India.
[2]Department of Chemistry, Government College Kharkhara, Rewari, Haryana, 123106, India.
[3]Department of Chemistry, RPS Degree College, Balana, Mahendergarh, Haryana, 123029, India.
[4]Department of Physics, RPS Degree College, Balana, Mahendergarh, Haryana, 123029, India.
*Corresponding author E-mail: yash.pf@gmail.com, njitendrag127@gmail.com

http://dx.doi.org/10.13005/ojc/400428

(Received: May 07, 2024; Accepted: July 19, 2024)

ABSTRACT

Transition metal disulfides (MS_2; M = Mo and W) nanostructures were successfully synthesized by a hydrothermal methodology based on the reaction between transition metal (Mo/W) and S sources at 240 ^{O}C for 24 hours. Detailed structural, morphological and optical analyses were performed using XRD, TGA/DSC, FESEM/EDX, HRTEM and UV-Vis spectroscopy. Gross structural investigations reveal that the crystalline nature of MS_2 materials with flake-like and rod-like morphologies. MoS_2 in 2D flake-like morphology with thickness of about 15 nm (± 2nm) and WS_2 in 1D rod-like morphology with width between 7-9nm (±0.5nm) were achieved. The UV-Vis spectroscopy data elucidate two different optical band gaps 1.88 eV and 2.29 eV were achieved for MoS_2 nanoflakes, and for WS_2 nanorods it was 1.84 eV. The simple and cost-effective synthesis approach with detailed microstructure analyses and optical properties indicate a great potential of nanostructured MoS_2 and WS_2 as a vital component in new-generation semiconductor and optoelectronics devices.

Keywords: MoS_2, WS_2, Hydrothermal, Crystal structure, Microstructure, Optical.

INTRODUCTION

Nanostructured transition metal disulfides (TMDSs) have stimulated extensive attention of scientists and technologists for their exotic physical, structural, chemical, thermoelectric, tribological, mechanical and phase-dependent electronic properties that are useful for photodetectors, optoelectronics, spintronics, light-emitting devices, energy- and hydrogen-storage applications[1-9]. Amongst various TMDDs, Mo and W-based TMDSs (MoS_2 and/or WS_2; Mo/WS_2) nanostructures in recent years have been promising as innovative interesting materials. Depending on the coordination of transition metal (Mo/W) atoms with sulfur (S) atom, nanostructured Mo/WS_2 can be stable or metastable and they poses metallic, semiconductor or superconductor behaviour. For example, both Mo/WS_2 elucidate an octahedral coordination and a prismatic coordination for the metal atom denoting as 1T- and 2H-structure, respectively; in which metastable 1T-Mo/WS_2 is metallic, stable 2H-Mo/

WS_2 is semiconductor and 2M-WS_2 exhibits intrinsic superconductivity[9-11]. Moreover, Mo/WS_2 materials contain a lamellar structure and exhibit layer-dependent optical band-gap[12-13]. Owing to the layered structure, the use of Mo/WS_2 as electrode materials can substantially improve the supercapacitor performances[14-15]. The rich and unusual prerogatives of Mo/WS_2, therefore, are making them efficiently multifunctional materials in diverse fields of cutting-edge scientific research. In fact, two-dimensional (2D) and one-dimensional (1D) nanostructured MoS_2 and WS_2 establish for a variety of potential applications such as photo-synaptic transistor, photocatalytic hydrogen evolution, optoelectronic, phtotdetectors, lithium-, sodium- and magnesium-ion batteries, supercapacitors and sensors[2-3,7-9,13, 15,30].

Interestingly, the fascinating properties of Mo/WS_2 are strongly dependent on their atomic compositions and structures, crystallinity, morphologies and sizes, which can be easily modified during adopted synthetic methods. Many efforts based on chemical and/or physical approaches have been proposed for growing such newly emerging Mo/WS_2 materials with different morphologies ranging from three-dimensional (3D) to 2D to 1D system. Notably, colloidal synthesis, chemical vapour deposition, sonochemical treatment, substrate growth, microwave, catalyzed transport, hydrothermal and exfoliation methods have extensively been employed for synthesizing Mo/WS_2 nanosystems[5-7,16-19]. Amongst, hydrothermal methodology is a facile and low-cost approach attributed with miniaturized instrumentation[4,15,20-23]. Although hydrothermal synthesis has various advantages, however, it is still a great challenge to produce controllable and scalable Mo/WS_2. The results, so far, based on hydrothermal processing of Mo/WS_2 usually reported either complex reaction conditions inclusive of high temperature, long time duration, pH value or by using organic and/or inorganic surfactants[24-29]. That is being the case, the produced nanostructured Mo/WS_2 having non-stoichiometry, irregular shape, poor quality and low crystallinity. There is a strong structural requirement, thus, to develop Mo/WS_2 nanostructures in meticulous controlled growth with high-crystallinity and good-quality through a surfactant- and hazard-free hydrothermal method with non-involvement of complex chemical reaction conditions.

In this regard, the facile hydrothermal methodology based on the reaction between Mo/W and S sources at 240 ^{O}C for 24 h, is opted for synthesis of MoS_2 nanoflakes and WS_2 nanorods. The as-synthesized Mo/WS_2 nanostructures were characterized by X-ray diffraction (XRD), thermogravimetric analysis (TGA) and differential scanning calorimetry (DSC) scans, field emission electron microscopy (FESEM), energy dispersive X-ray (EDX), elemental mapping, high-resolution transmission electron microscopy (HRTEM) and UV-Vis spectroscopy techniques. The overall structural analyses revealed that the as-prepared MS_2 materials were crystallized in 2H-Mo/WS_2 structure and self-assembled in 2D flake-like and 1D rod-like morphologies. Electron microscopy studies signifies the 2D flake-like morphology with thickness of about 15nm (±2nm) and 1D rod-like morphology with width ranging from 7nm to 9nm (±0.5nm) of MoS_2 and WS_2 nanostructures, respectively. The consequences from UV-Vis spectroscopic data assure the absorbance capability over a large wavelength range of UV-Visible range. Two distinct band transitions for MoS_2 nanoflakes are indicated by two different optical band gaps appeared at 1.88 eV and 2.29 eV, whereas single band transition achieved at 1.84 eV for WS_2 nanorods. The facile hydrothermal strategy, detailed microstructural and optical properties analyses, therefore, indicate a potential candidature for both MoS_2 and WS_2 nanostructures as a vitally important component in functional devices.

EXPERIMENTAL

Materials

Ammonium molybdate tetrahydrate ($(NH_4)_6Mo_7O_{24}.4H_2O$; ACS, 81-83% MoO_3 basis, Sigma Aldrich) and tungsten hexachloride (WCl_6, ≥99.9% purity, trace metals basis, Sigma-Aldrich) were used as Mo and W sources, respectively. Thiourea (CH_4N_2S; ACS, 99%, Merck) and thioacetaamide (TAA; C_2H_5NS, 98% purity, reagent grade, Sigma-Aldrich) were used as sulfur (S) source for processing of MoS_2 and WS_2, respectively. All the chemicals were used as-received without any further purification. Absolute ethanol (C_2H_5OH; AR, 99.9%) and Millipore water (18 MΩ.cm) were used as solvents throughout the experiments.

Synthesis of MoS_2 nanoflakes morphology

The synthesis procedure for MoS_2 nanoflakes was carried out by a hydrothermal method. In this process, initially $(NH_4)_6Mo_7O_{24}.4H_2O$ (12 mmol) was dispersed in 70 mL Millipore water (Mw) and then dispersed solution magnetically stirred vigorously to form a uniform transparent dispersion at room temperature (RT). About fifteen-fold higher molarities of CH_4N_2S (180 mmol) was added and further stirring followed to ensure a clear homogenous solution. The solution was then subjected to hydrothermal treatment at 240 °C for 24 h in a Teflon-containing stainless-steel autoclave kit. The obtained black/lead-gray colour material was washed properly with Mw and ethanol and was subsequently dried in vacuum at 100 °C for 12 hours.

Synthesis of WS_2 nanorods morphology

WS_2 nanorods were also carried out by a hydrothermal method through a slight modification in precursor quantity but same hydrothermal reaction conditions. Firstly, 2 mmol of WCl_6 was dissolved in 35 Mw (half-fold of initially Mw taken in MoS_2 synthesis) under vigorously stirring at RT. About ten-fold higher molarities of TAA (20 mmol) was added and further stirring to obtain a clear homogenous solution. Afterwards, the hydrothermal reaction conditions were kept same as in MoS_2 synthesis. The obtained light-blue colour material was washed properly with Mw and ethanol and was subsequently dried in vacuum at 60 °C for same time as previously for MoS_2 production. The synthesis procedure for preparing MoS_2 and WS_2 nanostructures has been schematically presented in Scheme 1.

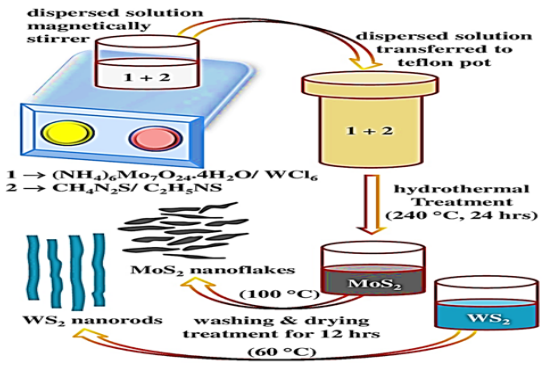

Scheme 1. Schematic illustration for the hydrothermal processing at 240 °C for 24 h of MoS_2 nanoflakes and WS_2 nanorods

Materials Characterizations

The phase- and crystal-structure analysis of the as-synthesized MoS_2 and WS_2 products were detected by X-ray diffraction (XRD) technique via a PAN analytical X'pert pro, Netherlands diffractometer using monochromatized Cu-Kα1 radiation (λ = 1.54 Å). Thermogravimetric analysis (TGA) and Differential scanning calorimetry (DSC) was used to perform the variation of weight and heat employing a Shimadzu DTG-60H thermoanalyzer instrument) under air flow. The sample (3.70 mg) was heated from room temperature (30 °C) to 700 °C at a linear heating rate of 10°C/minute. The morphology information and elemental analysis were determined by Tescan Maia3 Field-emission electron microscope (FESEM) operating at 10.0 kV coupled with an energy-dispersive X-ray spectroscopy (EDS, Oxford ULTI MAX 65) detector. Further microstructure characterization at high magnification and lattice fringe spacing analysis were carried out via transmission electron microscope (TEM) images recorded on a high-resolution TEM (HRTEM, JEOL 2100+, Japan) operating at an accelerating voltage of 200 kV. Optical band properties were studied via UV-Vis diffuse reflectance spectra (DRS) recorded by Cary-5000 UV-Vis-NIR spectrophotometer.

RESULTS AND DISCUSSION

Crystal Structure Identification by XRD and TG-DSC analysis

To elucidate the crystalline nature and phase analysis of MoS_2 nanoflakes, XRD studies have been carried out for as prepared black/lead-gray powder, as shown in Fig. 1 (a; upper segment). The XRD pattern was characterized by an intense and relatively broad diffraction peak at Bragg diffraction angle (2θ) value of about 14.37°, which can be assigned to those of the (002) lattice planes of a hexagonally symmetric 2H-phase of MoS_2 (2H-MoS_2) material. The other smaller diffraction peaks were located at 2θ values of about 33.51°, 39.55°, 49.51°, 58.67°, 60.10° and 70.13°, respectively, corresponding to the (101), (103), (105), (110), (008) and (108) lattice planes of MoS_2 material. All of these peaks with respect to their positions and relative intensities are in good agreement with the 2H-MoS_2 (space group: P63/mmc; standard JCPDS card no. 00-37-1492; a = b = 0.316nm,

c = 1.229nm, $\alpha = \beta = 90^{o}$ and $\gamma = 120^{\circ}$; unit cell volume V = 0.106 nm^3), which is composed by two MoS_2 layers per unit cell. No additional noticeable peak from impurities was detected in any of the material, indicating that the produced nanoflakes were of high crystalline and purity. However, the strongest peak of (002) planes at around 2 = 14.37° with interlayer spacing of about 0.616nm (obtained by Brass's equation: $2d\sin\theta = n\lambda$) is expressive of the structure being dominated by the long range layered structure. Additionally, the relatively higher intensity peak centered at 14.37° with full width at half maxima (FWHM, obtained by nonlinear curve fitting: Gauss fit) value of about 0.81 was used for calculating of average crystallite size employing Debye-Scherrer's equation. The estimated average crystallite size was 9.76nm for MoS_2 particles. Also, the broadening and relatively diminutive intensity of the subsequent peaks indicate the formation of MoS_2 nanoparticles. Fig. 1(b) illustrates the weight loss in TGA curve included with an exothermic peak in DSC curve of MoS_2 material within the temperature range of 30-700 °C under air atmosphere. The thermal decomposition and stability of MoS_2 was evaluated by TGA; there are three TGA regions in curve. From the TGA plot the total weight loss of MoS_2 of about 20.37% was observed when it was heated to 700 °C. For MoS_2, the initial weight loss of 3.76% up to 275 °C attributed to the thermal desorption of surface adsorbed CO_2 and moisture. The rapid weight loss from 280-460 °C indicates the drastic conversion of MoS_2 from precursors in this condition in accordance with the synthesis reactions[30-31]. The lower segment of Fig. 1(a) elucidates the XRD pattern of as-obtained WS_2 sample, which indicate that the synthesized WS_2 is crystalline. In XRD pattern, the peaks are observed at 2θ values of about 13.91°, 28.02°, 33.92°, 36.97°, 44.62°, 49.55°, 55.39°, 58.04° and 63.41° which can be well indexed with (002), (004), (101), (103), (006), (105), (106), (110) and (107) crystal lattice planes hexagonal phase of WS_2 (2H-WS_2), respectively. This is well consistent with the standard JCPDS card no. 00-008-0237 (space group: P63/mmc; a = b = 0.315nm, c = 1.236nm, $\alpha = \beta = 90^{o}$ and $\gamma = 120^{o}$; unit cell volume V = 0.106nm^3). No other diffraction peaks corresponding to any impurities of phase are detected, which signify that the hydrothermal processed WS_2 has a high purity and crystalline nature. Moreover, the relatively two higher intensity peaks centered at 13.91° and 28.02° with FWHM obtained by nonlinear curve fitting (Gauss fit) value of about 0.257 and 0.266 was used for calculating of crystallite size employing Debye-Scherrer's equation. The estimated crystallite size was 30.76nm and 30.41nm, respectively for WS_2 particles.

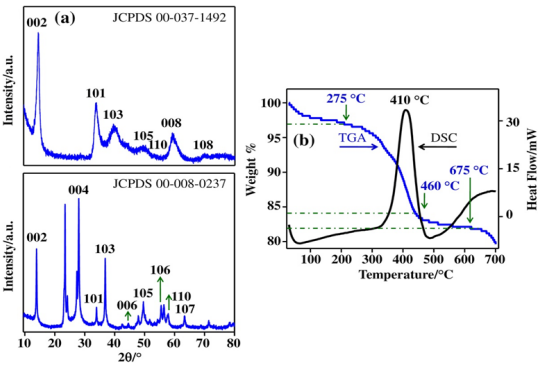

Fig. 1. Powder XRD pattern (a) of MoS_2 nanoflakes (upper segment) and WS2 nanorods (lower segment), (b) TGA-DSC curves of MoS_2 nanoflakes

Morphology analysis by electron microscopy

The morphology, chemical characteristics and microstructure of hierarchical flower-like MoS_2 nanostructures were assessed by FESEM-EDAX, TEM and high-resolution TEM (HRTEM) measurements. The surface morphology of MoS_2 sample could be clearly observed from both low and high magnification typical FESEM images. In low magnification FESEM image (Fig. 2(a)), MoS_2 demonstrates a three-dimensional (3D) flower-like morphology grown over and uniformly covering the entire surface with diameter range 0.8-1.2 μm (as indicated by white dotted circles and numerical symbols as 1 to 4), made of a layered two-dimensional (2D) nanoflakes. From the high-magnification image in Fig. 2(b), the ultrathin layered nanoflakes are clearly visible with thickness of around 35nm (±2nm) and lateral dimension ranging approximately from 200-300nm (±10nm), as marked with white dotted square and symbolized as numeric digits 1 and 2. The chemical characteristics especially elemental-composition and -distribution were analyzed using EDS and elemental mapping

(as shown in Fig. 2(c)-(e)) elucidating the absence of impurities in as-produced MoS_2 nanoflakes. From the EDS compositional analysis, corresponding spectrum is provided in Fig. 2(c), the presence of Mo and S elements confirms the formation of MoS_2, no other element was detected. The content of Mo and S for this sample to be 32.7% and 67.3% giving an atomic content $MoS_{2.05}$, as determined by EDS spectrum. The elemental mapping (Fig. 2(d)-(e)) reveals uniform distribution of Mo and S elements, especially, blue and red colour, respectively in MoS_2 nanoflowers. The microstructure properties of the prepared materials were further evaluated through TEM and HRTEM analyses (Fig. 2(f)-(g)), which distinctly observe the MoS_2 nanostructures. From the typical bright-field low magnification TEM image of the prepared MoS_2 sample (Fig. 2(f)), the formation of flower-like nanostructure with similar 3D surface morphology is observed, the average diameter is elucidated to be in range between 65 to 120nm (±5nm) by an assembly of 2D flake-like structure with thickness of about 15nm (±2nm, as indicated by yellow solid arrow) and their length could be estimated to be in 30-80nm (±3nm) region. The TEM image further reveals that the MoS_2 nanoflakes grown in one direction along their axis (as shown by yellow dotted arrow). A high resolution lattice scale HRTEM micrograph of nanoflakes has been produced in Fig. 2(g) and the 2D flake-like nanostructure was clearly visible with thickness of about 17nm (±2nm) throughout the sample, which is close agreement with the FESEM result, identifying that the synthesized nanoflakes have good crystallinity. The HRTEM image obviously provides the dominant presence of clear regular interplaner spacing along c-axis was estimated to be 0.62nm that corresponds to the (002) lattice plane of 2H-MoS_2 crystal structure, which is further validated by XRD analysis. A part of intrinsic structural one-dimensional defect (line imperfection) particular dislocation can be viewed (as indicated by yellow dotted lines in Fig. 2(g)), which probably attributed to a direct consequence of inconsistent accumulation of nanocrystals and expanded short-range ordering lattice formation.

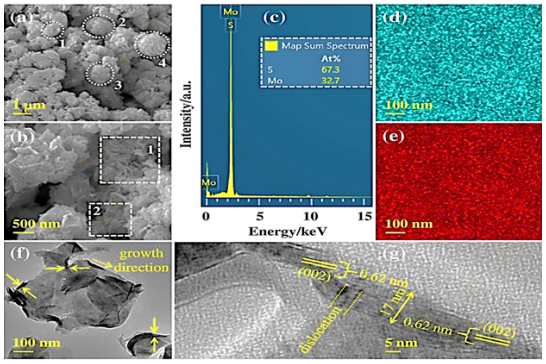

Fig. 2. FESEM images with low (a) and high magnification (b), EDAX spectrum (c) showing the presence of Mo and S elements in the sample, elemental mapping (d) and (e) of the elements Mo and S, respectively, bright-field low magnification TEM micrograph (f) and HRTEM image (g) of MoS_2 nanoflakes constituting hierarchical flower-like morphology

The EM images of as-prepared WS_2 sample are displayed in Fig. 3. The low magnification FESEM image (Fig. 3(a)) of the 2H-WS_2 sample, which consists of aggregates of uniform, straight and smooth one-dimensional (1D) rod-like structure, indicating that the well-organized controllable distribution with high-yield production can be achieved through this facile and cost-effective hydrothermal approach. Moreover, a high-magnification FESEM image (Fig. 3(b)) elucidates the large-scale production of nanorods with width of about 40nm (±5nm) and length of 230-360nm (±10nm). Bright-field low magnification TEM image in the Fig. 3(c) reveals additional information about the morphology and structure of the 2H-WS_2 nanorods. The nanostructured WS_2 clearly exhibits an aggregate of rod-like morphology in TEM image with width ranging from 7nm to 9nm (±0.5nm), as marked with red solid lines in different regions. The FESEM and TEM images clearly demonstrate the formation of WS_2 nanorods with uniform size distribution.

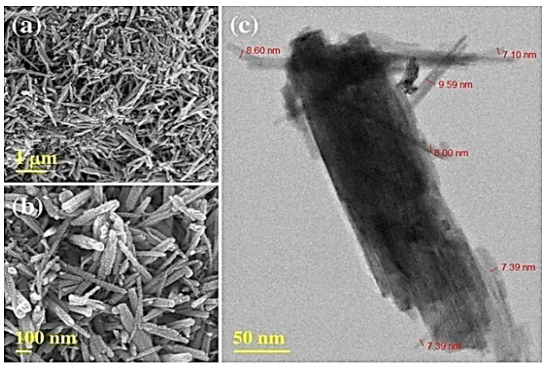

Fig. 3. FESEM images with low (a) and high magnification (b), and a bright-field low magnification TEM micrograph (c) of WS2 nanorods

Optical band analysis by UV-Vis spectroscopy

To investigate the optical behaviour of MoS_2 nanoflakes and WS_2 nanorods, UV-Vis absorption spectroscopy measurements were carefully evaluated, as displayed in Fig. 4-5. The optical UV-Vis absorption spectrum of prepared MoS_2 nanoflakes (main image, Fig. 4) is characterized by absorption peak maxima, which exhibits the absorbance capability in the visible light region from 340nm to 700nm. The obtained UV-Vis spectrum indicates that the MoS_2 nanoflakes has three absorption peaks obtained at about 348, 605 and 657nm that could be conceived to the different absorption sites of the material. The presence of different exciton absorption peaks is further the authentication of substantial quantum confinement effect[32]. Two different optical band gaps, 1.88 eV and 2.29 eV were determined from the corresponding Tauc plot (inset, Fig. 4) signifying the appearance of two distinct band transitions. These band gaps originate due to the electron transition between the valence bands Mo-3d, essentially the highest occupied molecular orbit (HOMO), and the conduction bands Mo-3d and S-p, essentially the lowest unoccupied molecular orbit (LUMO). The UV-Vis results are in good agreement with the theoretical and/or experimental results reported previously for 2H-MoS_2, which was expected[33].

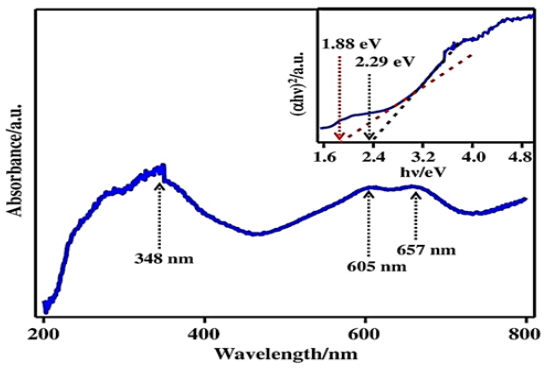

Fig. 4. UV-Vis absorbance of MoS_2 nanoflakes, inset shows the corresponding Tauc plot

The absorbance spectrum of 2H-WS_2 nanorods synthesized by hydrothermal approach processed at 240°C for 24 h is depicted in Fig. 5. It can be observed that the UV-Vis absorption spectrum shows an absorption peak about 276nm (4.49 eV). Interestingly, it is noted that the 2H-WS_2 nanorods have an observable absorption in the UV region, which can be considered the WS_2 nanorods as in UV photodetecter applications. The inset provides the energy band-gap value corresponds to the intercept of the straight-line of the plot with hν axis about 1.84 eV, which is in good agreement with the reported values[7,24,32].

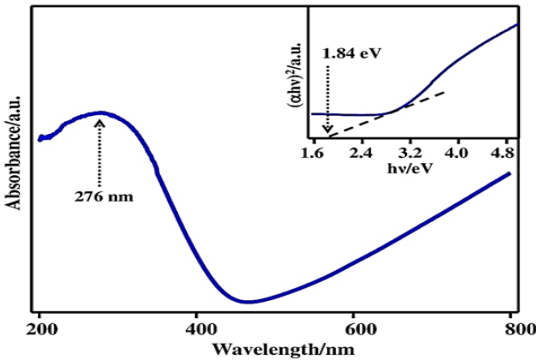

Fig. 5. UV-Vis absorbance of WS_2 nanorods, inset shows the corresponding Tauc plot

CONCLUSION

In conclusion, MoS_2 nanoflakes and WS_2 nanorods have been successfully prepared by hydrothermal synthesis at 240 °C for 24 hours. The as-synthesized Mo/WS_2 nanostructures have been well characterized by XRD, DSC-TGA, FESEM, EDX, elemental mapping, HRTEM and UV-Vis spectroscopy techniques. The crystal structural analysis revealed that the MS_2 materials have been crystallized in 2H-Mo/WS_2 phase. 2D flake-like and 1D rod-like morphologies have been identified using electron microscopy. The 2D flake-like morphology grew with thickness of about 15nm (±2nm), whereas 1D rod-like morphology with width ranging between 7 and 9nm (±0.5nm). The UV-Vis spectroscopy of Mo/WS_2 exhibits a promising absorbance capability in wavelength regime UV-Visible range. Moreover, distinct optical band gaps obtained at about 1.88 eV and 2.29 eV elucidating two different band transitions in MoS_2 nanoflakes, while a single band transition occurred at about 1.84 eV in WS_2 nanorods. The scalable hydrothermal technique and detailed crystal- and micro-structure characteristics with optical band properties altogether infer that the MoS_2 nanoflakes and WS_2 nanorods being a potential candidate opens the new paths for producing semiconducting and optoelectronics devices.

ACKNOWLEDGEMENT

JG would like to acknowledge the support of the SERB-DST sponsored project

(ECR/2017/000879; Diary No./Finance No. SERB/F/7840/2018-2019).

Conflict of Interest

The authors declare no conflict of interest.

REFERENCES

1. Wu, T.; Wang, C.; Hu, G.; Wang, Z., *Nat. Commun.*, **2024**, *15*, 3295. DOI: 10.1038/s41467-024-47610-z.
2. Park, J.; Kim, J. O.; Kang, S. W., *Sci. Rep.*, **2024**, *14*, 6922. DOI: 10.1038/s41598-024-57642-6.
3. Archana, B.; Kottam, N.; Nayak, S.; Chandrasekhar, K. B.; Sreedhara, M. B., *J. Phys. Chem.* C **2020**, *124*, 14485-14495. DOI: 10.1021/acs.jpcc.0c03411.
4. Padash, M.; Maghsoudi, S.; Mousavi, M., *Sci. Rep.*, **2023**, *13*, 8902. DOI: 10.1038/s41598-023-36028-0.
5. Vattikuti, S. V. P.; Byon, C., *J. Nanomater.*, **2015**, 2015, 710462. DOI: 10.1155/2015/710462.
6. Kobayashi, Y.; Sasaki, S.; Mori, S.; Hibino, H., *ACS Nano.,* **2015**, *9*, 4056-4063. DOI: 10.1021/acsnano.5b00103.
7. Mahler, B.; Hoepfner, V.; Liao, K.; Ozin, G. A., *J. Am. Chem. Soc.*, **2014**, *136*, 14121-14127. DOI: 10.1021/ja506261t.
8. Amani, M.; Lien, D. H.; Kiriya, D.; Xiao, J., *Science.,* **2015**, *350*, 1065. DOI: 10.1126/science.aad2114.
9. Coleman, J. N.; Lotya, M.; O'Neill, A.; Bergin, S. D., *Science.,* **2011**, *331*, 568-571. DOI: 10.1126/science.1194975.
10. Fang, Y.; Pan, J.; Zhang, D.; Wang, D., *Adv. Mater.*, **2019**, *31*, 1901942. DOI: 10.1002/adma.201901942.
11. Xing, Q.; Zhang, J.; Fang, Y, Song, C., *Nat. Commun.*, **2024**, *15*, 2623. DOI: 10.1038/s41467-024-46963-9.
12. Maharaj, D.; Bhushan, B., *Tribol. Lett.*, **2013**, *49*, 323-339. DOI: 10.1007/s11249-012-0071-0.
13. Kern, J.; Trügler, A.; Niehues, I.; Ewering, J., *ACS Photonics.,* **2015**, *2*, 1260-1265. DOI: 10.1021/acsphotonics.5b00123.
14. Song, Y.; Bai, S.; Zhu, L.; Zhao, M., *ACS Appl. Mater. Interfaces.*, **2018**, *10*, 13606-13613. DOI: 10.1021/acsami.8b02506.
15. Pereira, A. O.; Miranda, C. R., *J. Phys. Chem.,* C **2015**, *119*, 4302-4311. DOI: 10.1021/jp510182u.
16. Peimyoo, N.; Shang, J.; Cong, C.; Shen, X., *ACS Nano.,* **2013**, *7*, 10985-10994. DOI: 10.1021/nn4046002.
17. Jiang, J.; Shen, Q.; Xue, P.; Qi, H., *Chemistry Select.*, **2020**, *5*, 354-359. DOI: 10.1002/slct.201903924.
18. Matte, H. S. S. R.; Maitra, U.; Kumar, P.; Rao, B. G., *Z. Anorg. Allg. Chem.*, **2012**, *638*, 2617-2624. DOI: 10.1002/zaac.201200283.
19. Remskar, M.; Mrzel, A.; Skraba, Z.; Jesih A., *Science.*, **2001**, *292*, 479. DOI: 10.1126/science.1059011.
20. Naik, R. L.; Narsaiah, T. B., *Mater. Today Proc.*, **2023**, *72*, 268-273. DOI: 10.1016/j.matpr.2022.07.266.
21. Naik, R. L.; Narsaiah, T. B.; Justin, P.; Kumar, A. N., *Mater. Sci. Eng.* B., **2023**, *298*, 116861. DOI: 10.1016/j.mseb.2023.116861.
22. Naik, R. L.; Narsaiah, T. B.; Justin, P., *Int. J. Nano Dimens.*, **2023**, *14*, 145-156 DOI: 10.22034/IJND.2022.1965246.2172.
23. Venkateswarlu, P.; Umeshbabu, E.; Kumar, U. N.; Nagaraja, P., *J. Colloid Interface Sci.*, **2017**, *503*, 17-27. DOI:10.1016/j.jcis.2017.05.007.
24. Cao, S.; Liu, T.; Zeng, W.; Hussain, S., *J. Mater. Sci.: Mater. Electron.*, **2014**, *25*, 4300-4305. DOI 10.1007/s10854-014-2164-z.
25. Nagaraju, C.; Gopi, C. V. V. M.; Ahn, J. W.; Kim H. J., *New J. Chem.*, **2018**, *42*, 12357-12360. DOI: 10.1039/C8NJ02822B.
26. Cao, S.; Liu, T.; Hussain, S.; Zeng, W., *Mater. Lett.*, **2014**, *129*, 205-208. DOI: 10.1016/j.matlet.2014.05.013.
27. Zhang, D.; Liu, T.; Jia, Y.; Chai, J., *Integr. Ferroelectr.*, **2018**, *188*, 24-30, DOI: 10.1080/10584587.2018.1454759.
28. Shelke, N. T.; Karche, B. R., *J. Alloys Compd.*, **2015**, *653*, 298-303. DOI: 10.1016/j.jallcom.2015.08.255.
29. Li, L.; Chen, J.; Wu, K.; Cao, C., *Nanomaterials.,* **2019**, *9*, 1366. DOI: 10.3390/nano9101366.
30. Kumar, N.; Siroha, P.; Sharma, Y.; Singh, D., *Appl. Surf. Sci. Adv.*, **2021**, *6*, 100167. DOI: 10.1016/j.apsadv.2021.100167.
31. Lin, C. H.; Tsai, C. H.; Tseng, F. G.; Yu, Y. Y., *Nanoscale Res. Lett.*, **2015**, *10*, 446. DOI: 10.1186/s11671-015-1156-0.
32. Kim, E. B.; Akhtar, M. S.; Ameen, S.; Umar, A., *Nano Energy.*, **2022**, *102*, 107673. DOI: 10.1016/j.nanoen.2022.107673.
33. Yang, K.; Liu, T.; Zhang, X. D., *Front. Chem.*, **2021**, *9*, 700250. DOI:10.3389/fchem.2021.700250.